2D Materials



12 April 2023

REVISED

28 May 2023

ACCEPTED FOR PUBLICATION 12 June 2023

PURI ISHED

29 June 2023

PAPER

Effect of environmental screening and strain on optoelectronic properties of two-dimensional quantum defects

Shimin Zhang^{1,2}, Kejun Li², Chunhao Guo^{1,3} and Yuan Ping^{1,2,*}

- Department of Materials Science and Engineering, University of Wisconsin-Madison, Madison, WI 53706, United States of America
- Department of Physics, University of California, Santa Cruz, CA 95064, United States of America
- Department of Chemistry and Biochemistry, University of California, Santa Cruz, CA 95064, United States of America
- Author to whom any correspondence should be addressed.

E-mail: yping3@wisc.edu

Keywords: first-principles, quantum defects, 2D materials, strain effect, substrate screening, many-body perturbation theory Supplementary material for this article is available online

Abstract

Point defects in hexagonal boron nitride (hBN) are promising candidates as single-photon emitters (SPEs) in nanophotonics and quantum information applications. The precise control of SPEs requires in-depth understanding of their optoelectronic properties. However, how the surrounding environment of host materials, including the number of layers, substrates, and strain, influences SPEs has not been fully understood. In this work, we study the dielectric screening effect due to the number of layers and substrates, and the strain effect on the optical properties of carbon dimer and nitrogen vacancy defects in hBN from first-principles many-body perturbation theory. We report that environmental screening causes a lowering of the quasiparticle gap and exciton binding energy, leading to nearly constant optical excitation energy and exciton radiative lifetime. We explain the results with an analytical model starting from the Bethe-Salpeter equation Hamiltonian with Wannier basis. We also show that optical properties of quantum defects are largely tunable by strain with highly anisotropic response, in good agreement with experimental measurements. Our work clarifies the effect of environmental screening and strain on optoelectronic properties of quantum defects in two-dimensional insulators, facilitating future applications of SPEs and spin qubits in low-dimensional systems.

1. Introduction

Point defects in two-dimensional (2D) materials have been found to possess outstanding quantum properties such as stable single-photon emission, and have been exploited as spin quantum bits (qubits) for quantum information technologies [1, 2]. The single-photon emitters (SPEs) in 2D materials are highly stable and tunable [2-4], and in particular, their optical activation can be spatially controlled and tuned by strain [5, 6], emphasizing the great potential of SPEs in 2D materials.

The defect candidates with promising quantum properties exhibit deep-level states or form a defect-bound exciton. A large number of defects in hexagonal boron nitride (hBN) have been proposed since the report by Tran et al [7]. So far, spin defect V_B has been unambiguously identified from experiment [8-11] and theory [12, 13]. Many of the other defects, whose atomic origins are yet to be determined, were found to be \sim 2 and \sim 4 eV SPEs [14–17]. From theoretical predictions, N_BV_N [7, 14], boron dangling bonds [18], C_BV_N [19, 20], and carbon trimers [21–24] were proposed to be defect candidates for the \sim 2 eV SPEs, while C_BC_N [25], C_NO_N [26], Stone-Wales defect [27], and carbon ring [28] were propsed for the \sim 4 eV SPEs.

Among the proposed defect candidates, only partial experimental observations can be explained. Most importantly, large variations of key physical properties including zero-phonon line (ZPL), photoluminescence lifetime, and Huang-Rhys factor [22, 29] were observed. The physical origin of such variation is undetermined, with only some plausible explanations. For example, it is speculated that different substrates or sample thicknesses used in experiments may lead to variation [7, 15, 30]. Strain can be another source for the variation, as indicated by the past experimental studies [14, 31, 32]. Natural strain can be introduced when placing materials on top of substrates.

Theoretically, first-principles computation has been a powerful tool for identifying and proposing new defects as SPEs and spin qubits in 2D materials [33]. However, different structural models including monolayer, multilayer or bulk hBN [13, 21–25] were used in different studies, which lead to difficulties in comparison with experiments and comparison among different theoretical studies. Furthermore, the effect of substrates has been mostly examined at the mean-field level by DFT with semilocal functionals, where excitonic effects are not considered [34–36]. Finally, the effect of strain on optical properties, such as absorption spectra, exciton binding energies, and radiative lifetime, has not been investigated to the best of our knowledge.

In this work, from first-principles calculations, we investigate the environmental screening effect due to the layer thickness and substrates, as well as the strain effect on the optoelectronic properties of point defects in hBN. In order to pick representative defects for general conclusions, we choose C_BC_N as an example of extrinsic substitutional defects and N_BV_N as an example of native vacancy defects, both of which are commonly found in hBN and previously proposed to be possible \sim 4 and \sim 2 eV SPEs, respectively. Our results provide an estimation of how sensitive the excitation energy, exciton binding energy, and ZPL are to strain, and we explain their qualitative trends through molecular orbital theory. We also provide intuitive and comprehensive understanding of the environmental screening effect on defect properties through both first-principles many-body perturbation theory calculations and analytical models.

2. Computational method

The ground state calculations are carried out by density functional theory implemented in the QuantumEspresso package [37], with the Perdew–Burke–Ernzerhof (PBE) exchange correlation functional [38]. We use the SG15 optimized norm-conserving Vanderbilt pseudopotentials [39, 40] and 80 Ry wave function kinetic energy cutoff (320 Ry charge density cutoff) for the plane wave basis set. The defect calculations are performed with a 6×6 supercell and $3 \times 3 \times 1$ k-point sampling, based on our convergence tests in previous studies [22, 31, 41].

We perform the many-body perturbation theory calculations with G_0W_0 (one-shot GW, G stands for Green's function and W stands for screened Coulomb interaction) starting from PBE electronic states for the quasiparticle energies, and solve the Bethe–Salpeter equation (BSE) for the optical properties [42] with excitonic effects by the Yambocode [43]. We note that in our previous work [44], we compared GW and hybrid functional calculations for the electronic structure of hBN and its point defects. We found G_0W_0 @PBE and the Koopmans-compliant hybrid functional give similar electronic structure for hBN and its point defects. The GW calculation is carried out with 8 Ry response block size and 1800 energy bands for the dielectric matrix and self-energy, while we use 5 Ry and 80 bands for the BSE kernel and optical spectra calculations. With the 2D Coulomb truncation technique [45], the quasiparticle energies are converged within 10 meV at 33.5 a.u. vacuum size. More details on convergence tests can be found in supplementary figures S1 and S2.

We then calculate the ZPL by subtracting the Frank–Condon shift $E_{\rm FC}$ from the BSE excitation energy, where the $E_{\rm FC}$ is obtained by the constrained DFT (cDFT) technique [41]. By taking the excitation energy and exciton dipole moment from the solution of BSE, we then evaluate radiative lifetime for defects in 2D systems derived from Fermi's golden rule, with $\tau_R = 3\pi\epsilon_0 h^4 c^3/n_D e^2 E^3 \mu^2$ [41, 46]. Here E is the exciton energy, c is the speed of light, μ^2 is the modulus square of the exciton dipole moment, and n_D is the reflective index, which is one for monolayer hBN.

For the study of layer thickness and substrate effects, we apply our recently developed sum-up effective polarizability ($\chi_{\rm eff}$ -sum) with the reciprocalspace linear interpolation technique, in order to account for the impact of substrates and multilayers [47, 48]. This method allows us to separate the total interface into two subsystems as substrate pristine layers and defective monolayer, allowing a large saving of computational cost and avoiding artificial strain from enforcing lattice matching at interfaces.

3. Results and discussion

3.1. Electronic and optical properties of defects in hBN

We start from a discussion of electronic structure and optical properties of defects in monolayer hBN, followed by a discussion of strain and layer thickness/substrate effects. We choose carbon dimer (C_BC_N) and nitrogen vacancy (N_BV_N) defects in hBN as our prototypical systems, both of which are common defects in hBN. In particular, C_BC_N was identified as a defect candidate for 4 eV SPE in hBN [49]. The atomic structures and electronic structures of C_BC_N and N_BV_N are shown in figures 1 and 2, respectively. The atomic structures show that both C_BC_N and $N_B V_N$ belong to the $C_{2\nu}$ point symmetry group. We label the defect wave functions according to the irreducible representations to which they transform (details of symmetry notation can be found in SI section III). In particular, the $1b_1$ and $2b_1$ states of

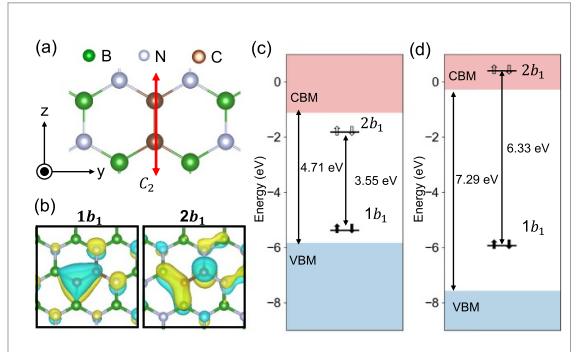


Figure 1. Structural and electronic properties of carbon dimer (C_BC_N) in hBN. (a) Atomic structure, (b) defect-related wave functions, and single-particle diagrams of the ground state at the level of (c) PBE and (d) $G_0W_0@PBE$. The zero energy is aligned to the vacuum level, and the defect states are labeled by their wave function symmetry based on the irreducible representation of the $C_{2\nu}$ symmetry group.

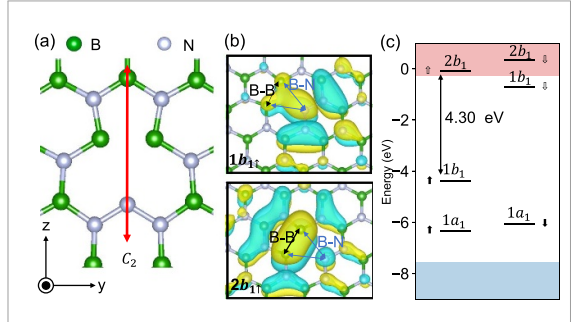


Figure 2. Structural and electronic properties of nitrogen vacancy (N_BV_N) in hBN with $C_{2\nu}$ symmetry. (a) Atomic structure, (b) defect-related wave functions, and (c) single-particle diagram of the ground state at the G_0W_0 @PBE level. The vacuum level and defect state notations are set up in the same way as C_BC_N .

 C_BC_N , and $1b_{1\uparrow}$ and $2b_{1\uparrow}$ states of N_BV_N are of interest (the symmetry notation of orbitals and the corresponding character table can be found in section III.A of the supplementary material), as they correspond to the optically allowed intra-defect transitions [31, 49]. The comparison between the electronic structures at PBE and G_0W_0 @PBE levels in figures 1(c) and (d) indicates that the quasiparticle correction shifts the occupied defect states downward and unoccupied states upward, opening up the defect gap of C_BC_N to 6.33 eV from 3.55 eV, and the defect gap of N_BV_N to 4.30 eV from 2.06 eV at PBE.

We then carried out BSE calculations for the related vertical excitation energy. The complete BSE spectra and the exciton wave function are presented in supplementary figures S3 and S4. We note that the electronic gap of monolayer hBN is obtained as 7.01 eV in this work, which is consistent with previous theoretical studies [50–52]. The optical gap by BSE is 6.01 eV, which is consistent with the \sim 6 eV experimental optical gap of hBN [53], considering that the bulk and monolayer hBN optical gaps are very similar as discussed in figure 7. The results of C_BC_N indicate the presence of a single isolated peak

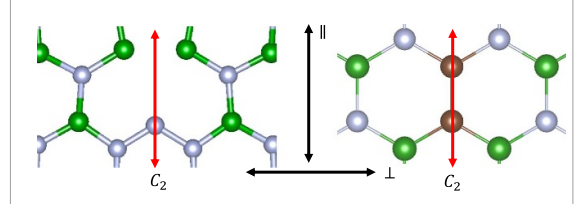


Figure 3. Directions of uniaxial strain along || and \bot to the C_2 axis.

related to the $1b_1 \rightarrow 2b_1$ transition at the BSE excitation energy ($E_{\rm BSE}$) of 4.44 eV, with a corresponding exciton binding energy of 1.89 eV and a radiative lifetime of 1.1 ns. The ZPL energy ($E_{\rm ZPL}$) was calculated to be 4.32 eV by subtracting the Franck–Condon shift ($E_{\rm FC}$) of 0.12 eV from the BSE excitation energy. This result is in agreement with previous studies, where a ZPL around 4.3 eV has been obtained using cDFT with hybrid functional [49] or GW&BSE with a finite-size cluster approach [54].

We acknowledge the intricate nature of local structural distortion and optical transition of the N_BV_N defect, and a related detailed discussion is presented in the supplemetary material, section VI. However, to keep the main text concise, we focus on the $1b_{1\uparrow} \rightarrow 2b_{1\uparrow}$ transition at $C_{2\nu}$ defect symmetry. The vertical transition energy for $1b_{1\uparrow} \rightarrow 2b_{1\uparrow}$ is 2.12 eV with a 57 ns radiative lifetime. The ZPL is 1.60 eV after subtracting the E_{FC} of 0.52 eV from the vertical transition by solving the BSE. Upon considering the transition to the lower symmetry ground state at C_s symmetry due to out-of-plane distortion, the ZPL energy increases to 1.70 eV. Our result for $1b_{1\uparrow} \rightarrow 2b_{1\uparrow}$ transition-related ZPL is lower than the previous calculation [5, 55] at hybrid functional, but consistent with previous BSE results of N_BV_N in C_s symmetry [56]. This highlights the important difference when the excitonic effect is taken into account.

3.2. Effect of strain

We investigate the effect of strain by applying it along two in-plane uniaxial directions, where the parallel (\parallel) strain denotes the strain along the C_2 axis, and the perpendicular (\perp) strain denotes the direction perpendicular to the C_2 axis (figure 3). The uniaxial strain here is defined as the stretching ratio of the lattice along a certain direction, with its magnitude as $\epsilon = (l-l_0)/l_0$, where l_0 and l are the lattice lengths before and after the strain is applied. ϵ denotes the macroscopic strain on the entire system. The strain tensor can thus be written as $\epsilon_{i,j} = \epsilon cos\theta_i cos\theta_j$ [6] where $\theta_i(\theta_j)$ is the angle between the strain axis and the ith(jth) coordinate direction (as defined in figures 1(a) and 2(a)).

Due to the $C_{2\nu}$ symmetry,the first-order response of the ZPL to the applied strain depends only on two in-plane diagonal components of the strain tensor,

2D Mater. 10 (2023) 035036 S Zhang et al

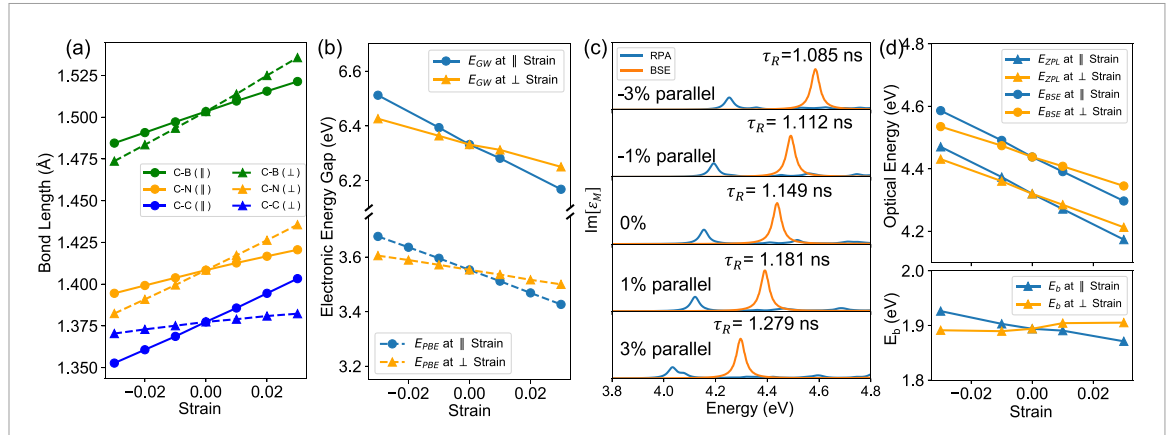


Figure 4. Strain effect on electronic and optical properties of the $1b_1 \rightarrow 2b_1$ transition at C_BC_N in hBN. (a) Bond length change of the C_BC_N defect as parallel (to C_2 symmetry axis, $\|$) and perpendicular (\bot) strain is applied. (b) Electronic energy gap change between defect states, including PBE and GW@PBE results along two directions of strain. (c) Optical spectra (only the energy range below the bulk-state transition is shown) are red-shifted as the strain increases at both random-phase approximation (RPA) level (blue) and BSE level (orange). The radiative lifetime is denoted as τ_R . (d) BSE excitation energy and ZPL energy (up), exciton binding energy (E_b, down) .

and thus can be written as (the detailed derivation can be found in the supplementary material, section III.B):

$$\Delta E_{\rm ZPL} = \epsilon (\kappa_{\parallel} \cos^2 \theta + \kappa_{\perp} \sin^2 \theta), \tag{1}$$

where θ is the angle between the strain axis and C_2 axis. The energy response to strain is quantified by two linear strain susceptibilities $\kappa_{\parallel(\perp)}$. In order to understand the determining factors on the ZPL energy change ($\Delta E_{\rm ZPL}$) when applying strain, $\Delta E_{\rm ZPL}$ can be decomposed into different contributions as follows:

$$\Delta E_{\rm ZPL} = \Delta E_{\rm PBE} + \Delta E_{\rm OP} - \Delta E_b - \Delta E_{\rm FC}, \qquad (2)$$

where ΔE_{PBE} is the change of DFT single-particle energy at the PBE level due to strain; ΔE_{QP} is the change of quasiparticle energy correction; ΔE_b is the change of exciton binding energy by solving the BSE; and ΔE_{FC} is the change of excited state relaxation energy (Franck–Condon shift) under strain.

We thus can separate the ZPL's strain susceptibility ($\kappa_{\rm ZPL}$) into terms corresponding to different levels of contribution from equation (2):

$$\kappa_{\mathrm{ZPL}}^{\parallel(\perp)} = \kappa_{\mathrm{PBE}}^{\parallel(\perp)} + \kappa_{\mathrm{QP}}^{\parallel(\perp)} - \kappa_b^{\parallel(\perp)} - \kappa_{\mathrm{FC}}^{\parallel(\perp)}. \tag{3}$$

By providing all the strain susceptibility components in equation (3), we can reveal the origin of the ZPL response to strain.

The effect of strain on the structural, electronic, and optical properties of C_BC_N in monolayer hBN is described in figure 4. Figure 4(a) displays the change in three bond lengths, including the defect–defect bond length (C–C) and the defect–nearest-neighbor bond lengths (C–N and C–B). All three bond lengths increase linearly with strain (where a positive sign denotes stretching strain and a negative sign denotes compressing strain). Figure 3(b) illustrates the change

in the defect electronic energy gap at the PBE level (E_{PBE}) and the G_0W_0 @PBE level (E_{GW}) . Figures 4(c) and (d) present the optical properties of the defect emitter, including the absorption peak related to $1b_1 \rightarrow 2b_1$ transition at RPA and BSE levels (c), and the corresponding BSE excitation energy (E_{BSE}) , ZPL (E_{ZPL}) , and exciton binding energy (E_b) as a function of strain (d). Both the optical and electronic energy gaps of the defect-related transition exhibit a linear red shift with increasing strain, with the parallel strain resulting in a larger response compared to the perpendicular strain. However, the radiative lifetime (τ_R) and exciton binding energy (E_b) show negligible response to the strain.

The linearity of response to strain in figure 4 suggests that the linear response model represented by equations (1) and (3) is adequate. As a result, the strain susceptibility and bond length change rate (R_{ν} , related to the local bond length change speed under strain, will be defined later) are summarized in table 1. Similar calculations were performed for the N_BV_N defect system and are summarized in the same table.

The results of ZPL strain susceptibility (κ_{ZPL}) reveal that the C_BC_N defect exhibits a similar negative strain susceptibility (red shift of ZPL) in both \parallel and \perp components, i.e. $\kappa_{\rm ZPL}^{\parallel} = -49.63~{\rm meV}\,\%^{-1}$ and $\kappa_{\text{ZPL}}^{\perp} = -36.49 \text{ meV } \%^{-1}$. On the other hand, the N_BV_N defect exhibits a disparate strain response behavior in two directions, where the | component of strain susceptibility is negative ($\kappa_{ZPL}^{\parallel} =$ $-105.20~{\rm meV\,\%^{-1}})$ and the \perp component is positive ($\kappa_{\rm ZPL}^{\perp} = 38.02 \text{ meV }\%^{-1}$). The sign difference in strain susceptibility reflects the different bonding nature of the defects as discussed later. By substituting the two components of strain susceptibilities into equation (1), one can determine the ZPL energy shift under any uniaxial strain in the linear response regime. Previous experimental work has shown that

Table 1. The bond length change rate (R) and strain susceptibilities (κ , with unit of meV $\%^{-1}$) of C_BC_N and N_BV_N under parallel ($\|$) and perpendicular (\bot) strain. The subscript of R denotes the atomic distance/chemical bond of interest, surrounding the defect center. The subscript of κ represents various contributions, i.e. 'QP' denotes quasiparticle correction; 'b' denotes exciton binding energy; 'FC' denotes Frank–Condon shift; 'ZPL' denotes zero-phonon lines.

C_BC_N										
	$R_{\mathrm{C-C}}$	$R_{\mathrm{C-B}}$	$R_{\mathrm{C-N}}$	$\kappa_{ exttt{PBE}}$	$\kappa_{ ext{QP}}$	κ_b	$\kappa_{ ext{FC}}$	$\kappa_{ m ZPL}$		
	0.613	0.301	0.411	-41.58	-15.70	-8.90	1.30	-49.63		
Ï	0.144	0.629	0.688	-17.75	-11.40	2.82	4.64	-36.49		
				N_BV_N	I					
	$R_{\mathrm{B-B}}$	$R_{\mathrm{B-N}}$	_	$\kappa_{ ext{PBE}}$	$\kappa_{ ext{QP}}$	κ_b	$\kappa_{ ext{FC}}$	$\kappa_{ exttt{ZPL}}$		
	0.463	1.664	_	-59.70	-19.32	-14.27	40.35	-105.20		
	2.072	0.490	_	44.96	1.00	2.05	6.31	38.02		

the uniaxial strain susceptibility of 2 eV SPE ranges from -120 to 60 meV $\%^{-1}$ without specifying the strain direction [6, 14, 57]. Therefore, our calculated strain response for the N_BV_N defect falls within the experimental strain susceptibility range [58] (more related discussion is detailed in the supplementary material).

Our analysis of κ_{ZPL} composition in table 1 indicates that the determining factors for strain response are different between the two defect systems. For the C_BC_N defect, the change from single-particle level at PBE and GW (κ_{PBE} and κ_{OP})is the dominant contribution, while exciton binding energy κ_b and the Frank–Condon shift κ_{FC} have a negligible impact. On the other hand, for the N_BV_N defect, although $\kappa_{\rm PBE}$ and $\kappa_{\rm QP}$ still dominate, the other contributions from κ_b and κ_{FC} have a sizable impact for $\kappa_{\rm ZPL}^{\parallel}$ (not for $\kappa_{\rm ZPL}^{\perp}$). Our analysis of the strain susceptibility highlights the importance of many-body effects and excited-state relaxation in determining the optical strain response. These factors impact both the magnitude and anisotropicity of the response. In light of these findings, it is crucial to consider these effects in the study of strain engineering for optical spectroscopy.

We then discuss the bond length change rate (R_{ν}) of local atomic distance ν (table 1) to identify the most relevant molecular orbitals responding to strain. The bond length change rate is defined as $(d_{\nu}-d_{0\nu})/(d_{0\nu})$, with $d_{0\nu}$ and d_{ν} as the local atomic distances before and after applying the strain. This quantity indicates to what extent the macroscopic tensile/compression strain can be transferred into the microscopic local structural change. This helps us develop insights into optoelectronic properties based on molecular orbital theory, given the localized nature of defect-related wave functions.

For example, in the C_BC_N defect system, the C–C bond has the largest change under parallel (\parallel) strain to the C_2 axis (therefore the largest R_{C-C}), which induces change to the corresponding molecular orbitals (MO) between two carbon atoms. From the defect wavefunctions in figure 1(b), we find that the lower defect level 1 b_1 has a π bonding character between

two C atoms; instead, the higher defect level $2b_1$ has a π^* antibonding character. As a result, the stretching of the C-C bond weakens charge density overlap between two C atoms, leading to a decrease of the energy gap between π (1 b_1) and π^* (2 b_1), shown as a red shift in figures 4(b) and (c). This change also results in a negative strain susceptibility in table 1. Similar discussions can be applied to the N_BV_N defect system; one exception is that the strain susceptibility is positive when applying strain perpendicular to the C_2 axis of the N_BV_N defect, where we find the B– B distance has the largest change (R_{B-B} close to 1). Interestingly, the highest occupied defect level $1b_1$ has a nearly non-bonding character between two B atoms, but the lowest unoccupied defect level $2b_1$ in the same spin channel has a bonding character between two B atoms. Stretching the B–B bond will decrease the charge density overlap between the two B atoms, which increases the energy of $2b_1$ but weakly affects $1b_1$. As a result, the energy gap between two defect levels is increased, which explains its positive κ along the \perp direction, opposite to the others in table 1.

In summary, our study analyzed the effects of strain on the electron and optical properties of hBN defects through the use of two representative systems: the carbon dimer defect C_BC_N and the nitrogen vacancy complex N_BV_N . Our calculations included both many-body effects and relaxation of excited states in determining the strain susceptibility of the ZPL. Our findings emphasized the importance of incorporating many-body contributions in studies of optical spectroscopy under strain. Additionally, we analyzed the different signs of strain response susceptibility through molecular orbital theory, after identifying the primary molecular orbitals responding to strain.

3.3. Layer thickness dependence and substrate

We next look at the layer thickness dependence and substrate effects on defect emitter properties. We use our implicit χ_{eff} -sum method [47, 48] to calculate the properties of one isolated defect within 1–3 layers (figures 5(a) and (b)) and bulk hBN (figure 5(c)). We

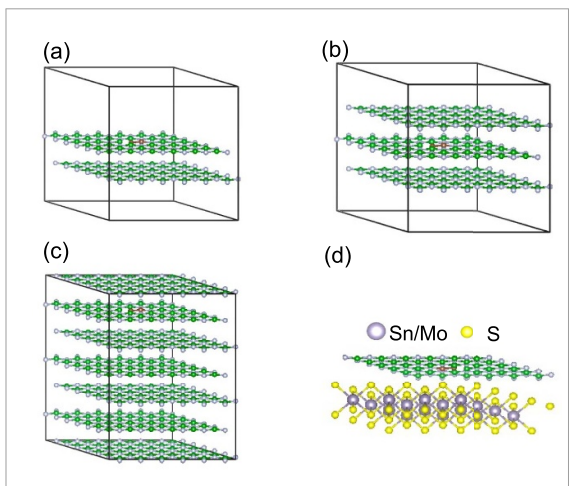
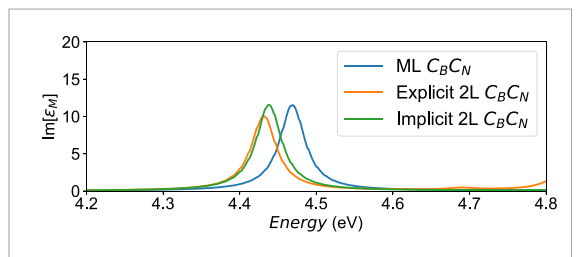


Figure 5. Lattice structures of (a) defect in double-layer hBN, (b) defect in three-layer hBN, (c) defect in bulk hBN, (d) defect in monolayer hBN on MoS₂ and SnS₂ substrates.



	$E_{\rm BSE}({ m eV})$	$\tau_R \; (\mathrm{ns})$	$E_{\rm GW}({ m eV})$	$E_b(eV)$
ML	4.469	1.1	6.336	1.867
Implicit	4.438	1.3	6.045	1.607
Explicit	4.431	1.3	5.958	1.527
Error(ImEx.)	0.007	< 0.01	0.087	0.080

Figure 6. Benchmark calculations of C_BC_N in two-layer hBN for χ_{eff} -sum implicit method. The figure shows the absorption spectra by solving the BSE. The table below the absorption spectra listed the BSE defect peak transition energy (E_{BSE}), radiative lifetime (t_R), electronic energy gap between defect states at GW@PBE level (t_R), and exciton binding energy of the defect peak (t_R). The errors (Error) are the difference of results obtained by implicit and explicit methods. We noticed there is an error cancellation between t_R and t_R and t_R .

choose the AA' stacking structure and set the interlayer distance to the bulk value of 3.33 Å [59]. For the substrate effect study, we choose two different transition metal dichalcogenides (TMD) materials as substrates (figure 5(d)) with layer distance to defective hBN of 3.31 Å for SnS₂ and 3.33 Å for MoS₂ substrates [47].

To validate the result from our implicit $\chi_{\rm eff}$ -sum method [47, 48], we compare its results with explicit bilayer calculations by using C_BC_N in hBN as an example. In figure 6, the panel above is the BSE absorption spectrum of defect-related peaks, where we show that explicit (orange) and implicit (green) two-layer calculations give similar results for the carbon-dimer defect, which are both red-shifted by 0.03 eV compared to the monolayer one (blue). The table appended to figure 6 summarizes the excitation energy ($E_{\rm BSE}$), electronic gap ($E_{\rm GW}$), and radiative

lifetime (τ_R) of the defect emitter, calculated from explicit and implicit interface methods.

We then show the results of layer thickness and substrate effects on optical spectra by using the implicit $\chi_{\rm eff}$ -sum method in figures 7(a) and (c). On increasing the number of layers or adding substrates, the position of defect peaks remains nearly constant, with a tiny shift (within 80 meV). The radiative lifetime (τ_R) also has negligible change. This result is consistent with experimental observations, where defect emitters did not change their ZPL energy either from 1L to 5L or with various substrates [60].

In figures 7(b) and (d), we show the layer thickness and substrate effect on the GW energy gap ($E_{\rm GW}$) and the exciton binding energy (E_b) of intra-defect transitions. A monotonic decrease of both $E_{\rm GW}$ and E_b has been observed with increasing layer thickness, where the changes nearly cancel each other, leaving the optical excitation energy unchanged ($E_{\rm opt} = E_{\rm GW} - E_b$). Interestingly, the substrate/layer effects on two defect emitters are similar; for example, for $C_{\rm B}C_{\rm N}$, $E_{\rm GW}$ decreases by 1.348 eV from monolayer to bulk, and for $N_{\rm B}V_{\rm N}$ it decreases by 1.370 eV. This finding indicates that the defect state energy renormalization by layer thickness and substrates weakly depends on the specific defects, but is mostly determined by the host environment.

We then qualitatively show that the energy renormalization of E_{GW} and E_b of defects is directly related to the environmental dielectric screening surrounding the defects, represented by total 2D effective polarizability ($\alpha_{2D,tot}$) [61, 62]. $\alpha_{2D,tot}$ can be calculated by summing up the 2D effective polarizability from each subsystem ($\alpha_{2D,tot} = \alpha_{2D,def} + \alpha_{2D,sub}$; 'sub' denotes substrate and 'def' denotes defected hBN monolayer), where the 2D effective polarizability of the subsystem is obtained by $\alpha_{2D} = (\epsilon - 1)$. $L/(4\pi)$. Here, L is the supercell lattice constant along the out-of-plane direction, and ϵ_{sub} is the in-plane component of the macroscopic dielectric tensor of the substrate calculated by density functional perturbation theory (DFPT) [63] (The dielectric constants are listed in the supplementary materials.) We then use the equation $E = A/\alpha_{2D,tot} + C$ to fit the relation between $\alpha_{2D,tot}$ and E_{GW}/E_b , with A and C the fitting parameters. The results are plotted in figure 7(e), which shows that an inversely proportional relation can well describe the E_{GW} and E_{b} dependence on environmental screening surrounding the defects (from both host hBN and substrates).

To better understand the insensitivity of the defect optical transition towards environmental screening, we present an analytic model for analyzing the renormalization of the defects' exciton binding energy (E_b) . Our analysis suggests that the stability of the defect spectroscopic peak position against the layer thickness and substrate is a result of two factors: (a) the high localization of the defect wave function and (b) the defect-related optical transition with no

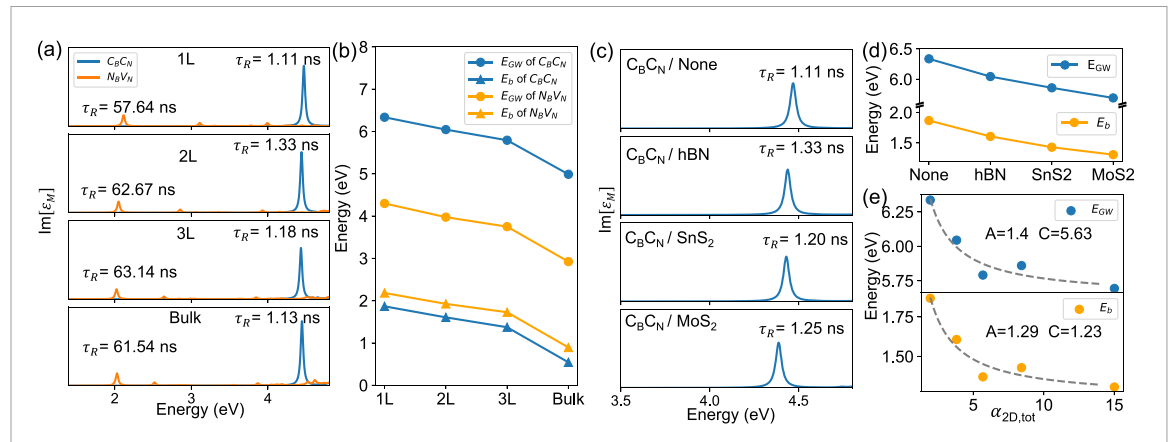


Figure 7. Layer thickness and substrate effect on electronic and optical properties. (a) The BSE peak of C_BC_N and N_BV_N defects with different layer numbers from 1L to bulk. (b) The exciton binding energy and GW energy of C_BC_N and N_BV_N defects as a function of layer thickness. (c) The BSE optical spectra of the C_BC_N defect in monolayer hBN on various substrates. (d) The exciton binding energy and GW energy gap of the C_BC_N defect in monolayer hBN on different substrates. (e) The GW energy and exciton binding energy as a function of total 2D polarizability ($\alpha_{2D,tot}$). The grey dashed line is the fitting result.

mixing with other transitions involving delocalized wave functions from the host, as discussed in detail below.

We start with the Hamiltonian for the BSE in Wannier basis [64]:

$$H^{S}(cv, c'v', \vec{R}) = E_{GW} \delta_{cc'} \delta_{vv'} - W_{vv'}^{cc'}(\vec{R}) + 2\delta_{S0} \sum_{\vec{R'}} \bar{V}_{v'c'}^{cv}(\vec{R'}) \delta_{\vec{R}0}, \quad (4)$$

where v/c are the pairs of occupied and unoccupied states, \vec{R} is the real-space lattice site, S is the spin, W is the screened exchange interaction between electron and hole (the direct term), \vec{V} is the exchange term from the Hartree potential, and $E_{\rm GW}$ is the GW electronic energy gap between c and v states. The Wannier function basis is obtained from the Fourier transform of the reciprocal-space Kohn Sham wave function to the real-space lattice:

$$a_{\nu/c}(\vec{x} - \vec{R}) = \frac{1}{G^{3/2}} \sum_{k} e^{-i\vec{k} \cdot \vec{R}} \phi_{\nu/c,k}(\vec{x}).$$
 (5)

The exciton energy and wavefunctions are obtained by diagonalizing the Hamiltonian:

$$\sum_{c'v'} H^{s}(cv, c'v') \phi_{\lambda}(c'v') = E_{\lambda} \phi_{\lambda}(cv), \qquad (6)$$

where ϕ_{λ} is the exciton wavefunction and E_{λ} is the exciton energy.

We consider the perturbation from the dielectric screening of pristine substrates or other pristine host material layers. (Notice that the inhomogeneous local dielectric environment from the host material around the defect is part of the unperturbed Hamiltonian.) The first-order perturbed change to the exciton energy E_{λ} is then:

$$\Delta E_{\lambda} = \langle \phi_{\lambda} | \delta \hat{H}^{s} | \phi_{\lambda} \rangle$$

$$= \sum_{C'} \sum_{c'v'} \langle \phi_{\lambda} \rangle cv \langle cv | \delta \hat{H}^{s} | c'v' \rangle \langle c'v' | \phi_{\lambda} \rangle, \quad (7)$$

where the matrix element of the perturbed Hamiltonian is:

$$\langle cv|\delta \hat{H}^{s}|c'v'\rangle = \delta H^{S}(c,v,c',v')$$

= $\delta E^{c,v}_{GW}\delta_{c,c'}\delta_{v,v'} - \delta W^{cc'}_{vv'},$ (8)

in which the first term is the renormalization of the electronic gap between the pair of c/v states. The second term is the change of screened exchange interaction, which contributes to the exciton binding energy change δE_b , defined as follows:

$$\delta E_b = \langle \phi_{\lambda} | \delta W | \phi_{\lambda} \rangle$$

$$= \sum_{c', c', v'} \langle \phi_{\lambda} | c v \rangle \langle c v | \delta W | c' v' \rangle \langle c' v' | \phi_{\lambda} \rangle. \quad (9)$$

Since the exchange term from the Hartree potential \bar{V} does not depend on dielectric screening, it does not appear in the perturbative Hamiltonian.

Here we consider defect-related Frenkel-like excitons, whose wavefunctions usually have components only from defect states, i.e. the $\langle \phi_{\lambda} \rangle cv$ is nonzero only when c and v are defect states. A previous study on the GW band gap renormalization effect of dielectric screening on benzene systems [65] (with the COHSEX model) has suggested that, when $\delta W(\vec{x},\vec{x}')$ is smooth and slowly varying over the spatial extension of the orbital, the GW energy gap renormalization can be approximated by $\delta E_{\rm GW}^{c,\nu} = P_{\nu} + P_{c}$, where $P_{c/\nu}$ is the static polarization integral for c/v state:

$$P_{c/\nu} = \frac{1}{2} \int d\vec{x} \int d\vec{x'} a_{c/\nu}(\vec{x}) a_{c/\nu}^*(\vec{x'}) \times \delta W(\vec{x}, \vec{x'}) a_{c/\nu}(\vec{x'}) a_{c/\nu}^*(\vec{x}).$$
(10)

2D Mater. 10 (2023) 035036 S Zhang et al

When defect orbitals are highly localized in real space, the integration can be reduced to the classical limit, where $P_{c/v} = \lim_{\rho \to 0} \delta W(\rho)$ [65, 66].

The same argument can be applied to the second term in equation (7), where the matrix element of two-particle screened Coulomb interaction change can be written as:

$$\delta W_{\nu\nu'}^{cc'}(\vec{R}) = \int_{U.C.} d\vec{x} \int_{U.C.} d\vec{x'} a_c^*(\vec{x}) a_{c'}(\vec{x})$$
$$\delta W(\vec{x} + \vec{R}, \vec{x'}) a_{\nu}(\vec{x'}) a_{\nu'}^*(\vec{x'}). \tag{11}$$

Since a single defect is not subject to a spatial periodicity, we can ignore the inter-site interaction and set $\vec{R}=0$. Then we rewrite the equation with two-electrons' distance $\rho=|x-x'|$, assuming the substrate screening being homogeneous in-plane (which is a reasonable approximation according to our past work [47]),

$$\delta W_{vv'}^{cc'} = \int_{U.C.} d\vec{x} \int_{U.C.} d\vec{x}' a_c^*(\vec{x}) a_{c'}(\vec{x})$$
$$\times \delta W(\rho) a_v(\vec{x}') a_{v'}^*(\vec{x}'). \tag{12}$$

Given localized (Frenkel) exciton, ρ is rather small or the exciton wavefunction is spatially confined. With an orthonormal condition of single-particle wavefunctions, we have

$$\delta W_{vv'}^{cc'} \approx \lim_{\rho \to 0} \delta W(\rho) \int_{U.C.} d\vec{x} \int_{U.C.} d\vec{x}'$$

$$a_c^*(\vec{x}) a_{c'}(\vec{x}) a_v(\vec{x}') a_{v'}^*(\vec{x}')$$

$$= \lim_{\rho \to 0} \delta W(\rho) \delta_{c,c'} \delta_{v,v'}. \tag{13}$$

Combining the discussions above for both terms in equation (8), we have $\langle cv|\delta \hat{H}^s|c'v'\rangle = 0$ when c and v are both defect single-particle states. Thus, the Frenkel-like exciton, composed of localized defect-defect transitions, will experience no change in the presence of substrate screening.

Finally, we apply a static model for $\delta W(\vec{x}, \vec{x}')$ derived from image charges [66] and compare with *ab initio* GW/BSE results. The environmental screening potential can be modeled as the potential energy of two charges in the defect layer (with dielectric constant ϵ_{def}) on top of substrate (with dielectric constant ϵ_{sub}) [66]. We assume the region above the defect layer to be a vacuum.

$$W(\vec{x}, \vec{x}') = W(\rho) = \frac{1}{\epsilon_{def}\rho} + 2\sum_{n=1}^{\infty} \frac{L_{12}^{n}}{\epsilon \{\rho^{2} + (2nd)^{2}\}^{1/2}} + L_{12}\sum_{n=0}^{\infty} \frac{L_{12}^{n}}{\epsilon (\rho^{2} + \{[(2n+1)d]^{2})\}^{1/2}},$$
(14)

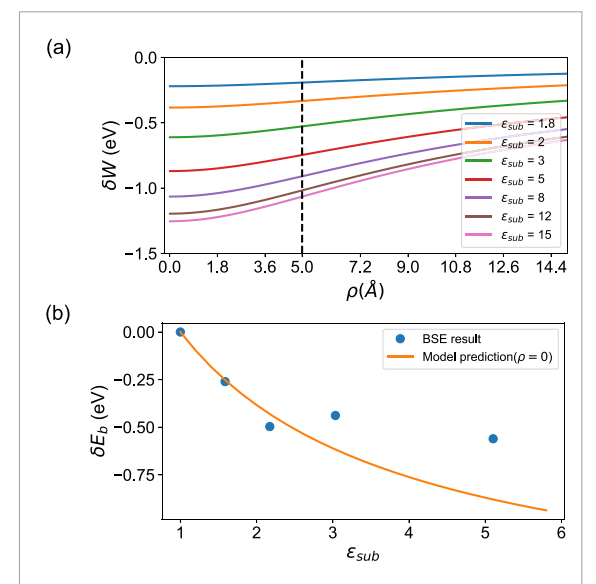


Figure 8. (a) The change of screened Coulomb potential as a function of electron–hole separation (ρ) at different substrate dielectric constants ϵ_{sub} . The calculation is performed using equations (14) and (15). The dashed line shows the localization range of the defect wave function where 99% of density lies within 5 Å. (b) The δE_b comparison of model prediction by using equations (9), (14) and (15) with results from full *ab initio* BSE. Good agreement between BSE results (blue dots) and model prediction (orange line) is obtained in the relatively low substrate dielectric constant range. In this range, δW varies more slowly, better satisfying the approximation in equation (12).

where d is the thickness of the defect layer, and $L_{12} = (\epsilon_{def} - \epsilon_{sub})/(\epsilon_{def} + \epsilon_{sub})$. We use the monolayer defect system without any substrate $(\epsilon_{sub} = 1)$ as the reference, then δW is defined as the change of W with and without substrates:

$$\delta W(\rho, \epsilon_{sub}) = W(\rho, \epsilon_{sub}) - W(\rho, \epsilon_{sub} = 1). \tag{15}$$

We plotted the change of screened Coulomb potential, $\delta W(\rho,\epsilon_{sub})$ in figure 8(a), where the defect layer thickness d=6.66 Å is extracted from inter-layer distance, and the defect layer dielectric constant ϵ_{def} is obtained in section VI of the supplementary information. The dashed line at 5 Å represents the maximum spanning range of the localized defect states $1b_1$ and $2b_1$.

Figure 8(b) shows that the δE_b calculated by equations (9), (14) and (15) compares reasonably well with *ab initio* BSE calculations (blue dots), especially in the low substrate screening regime. The underestimation of δE_b in the high dielectric constant of substrates ε_{sub} range may be due to an over-simplification of model W in equation (14). Nevertheless, the full *ab initio* GW/BSE calculation suggests that the cancellation effect for defect state transitions between exciton binding energy (δE_b) and GW quasiparticle energy renormalization ($\delta E_{\rm GW}$) still holds even at high substrate dielectric screening.

S Zhang et al

4. Conclusions

In this work, we have explored the impact of strain, layer thickness, and substrate effects on the electronic and optical properties of point defects in a 2D insulator—hBN. Our investigation takes into account the effects of many-body interactions and excited-state relaxation. We first analyzed various contributions to the strain susceptibility of ZPL, and found the dominant contributions often stem from changes at the single-particle level. We explained the ZPL shift direction under strain through molecular orbital theory, which is defect dependent, relying on the chemical bonding nature at the defect center.

Next our *ab initio* calculations demonstrated the robustness of the optical peak position of defect SPEs when varying the number of layers and substrates. We revealed the perfect cancellation between the renormalization of the quasiparticle energy gap and the exciton binding energy due to environmental screening. To further understand this result, we derived analytical models based on solving the BSE with Wannier basis for Frenkel excitons to reveal the underlying mechanism and the required condition, i.e. the localization nature of a defect-bound exciton. We then used a simple image-charge model for screened Coulomb potential to further validate such a cancellation effect.

Our findings provide in-depth insights into the mechanisms and conditions that control the environmental impact on the properties of quantum defects, and shed light on the emerging research on strain and substrate engineering of quantum defects in 2D materials.

Data availability statement

All data that support the findings of this study are included within the article (and any supplementary files).

Acknowledgments

We acknowledge the support by the National Science Foundation under Grant No. DMR-2143233. This research used resources of the Scientific Data and Computing center, a component of the Computational Science Initiative, at Brookhaven National Laboratory under Contract No. DE-SC0012704, the lux supercomputer at UC Santa Cruz, funded by NSF MRI Grant AST 1828315, the National Energy Research Scientific Computing Center (NERSC), a U.S. Department of Energy Office of Science User Facility operated under Contract No. DE-AC02-05CH11231, and the Extreme Science and Engineering Discovery Environment (XSEDE) which is supported by National Science Foundation Grant No. ACI-1548562 [67].

ORCID iDs

Shimin Zhang https://orcid.org/0000-0001-6319-148X

Yuan Ping https://orcid.org/0000-0002-0123-3389

References

- [1] Aharonovich I and Toth M 2017 Science 358 170
- [2] Liu X and Hersam M C 2019 Nat. Rev. Mater. 4 669
- [3] Wolfowicz G, Heremans F J, Anderson C P, Kanai S, Seo H, Gali A, Galli G and Awschalom D D 2021 Nat. Rev. Mater. 6 906
- [4] Yim D, Yu M, Noh G, Lee J and Seo H 2020 ACS Appl. Mater. Interfaces 12 36362
- [5] Li S, Chou J-P, Hu A, Plenio M B, Udvarhelyi P, Thiering G, Abdi M and Gali A 2020 npj Quantum Inf. 6 1
- [6] Mendelson N, Doherty M, Toth M, Aharonovich I and Tran T T 2020 Adv. Mater. 32 1908316
- [7] Tran T T, Bray K, Ford M J, Toth M and Aharonovich I 2016 Nat. Nanotechnol. 11 37
- [8] Gottscholl A et al 2020 Nat. Mater. 19 540
- [9] Gottscholl A, Diez M, Soltamov V, Kasper C, Sperlich A, Kianinia M, Bradac C, Aharonovich I and Dyakonov V 2021 Sci. Adv. 7 eabf3630
- [10] Gao X et al 2022 arXiv:2203.13184
- [11] Qian C et al 2022 arXiv:2202.10980
- [12] Reimers J R, Shen J, Kianinia M, Bradac C, Aharonovich I, Ford M J and Piecuch P 2020 Phys. Rev. B 102 144105
- [13] Ivády V, Barcza G, Thiering G, Li S, Hamdi H, Chou J-P, Legeza O and Gali A 2020 *npj Comput. Mater.* **6** 1 (available at: www.nature.com/articles/s41524-020-0305-x)
- [14] Grosso G, Moon H, Lienhard B, Ali S, Efetov D K, Furchi M M, Jarillo-Herrero P, Ford M J, Aharonovich I and Englund D 2017 Nat. Commun. 8 705
- [15] Mendelson N et al 2021 Nat. Mater. 20 321
- [16] Bourrellier R, Meuret S, Tararan A, Stéphan O, Kociak M, Tizei L H G and Zobelli A 2016 Nano Lett. 16 4317
- [17] Museur L, Feldbach E and Kanaev A 2008 Phys. Rev. B 78 155204
- [18] Turiansky M E, Alkauskas A, Bassett L C and Van de Walle C G 2019 *Phys. Rev. Lett.* **123** 127401
- [19] Sajid A and Thygesen K S 2020 2D Mater. 7 031007
- [20] Fischer M et al 2021 Sci. Adv. 7 eabe7138
- [21] Jara C, Rauch T, Botti S, Marques M A, Norambuena A, Coto R, Castellanos-Águila J, Maze J R and Munoz F 2021 J. Phys. Chem. A 125 1325
- [22] Li K, Smart T J and Ping Y 2022 Phys. Rev. Mater. 6 L042201
- [23] Golami O, Sharman K, Ghobadi R, Wein S C, Zadeh-Haghighi H, da Rocha C G, Salahub D R and Simon C 2022 Phys. Rev. B 105 184101
- [24] Maciaszek M, Razinkovas L and Alkauskas A 2022 Phys. Rev. Mater. 6 014005
- [25] Mackoit-Sinkevičienė M, Maciaszek M, Van de Walle C G and Alkauskas A 2019 Appl. Phys. Lett. 115 212101
- [26] Vokhmintsev A, Weinstein I and Zamyatin D 2019 J. Lumin. 208 363
- [27] Hamdi H, Thiering G, Bodrog Z, Ivády V and Gali A 2020 npj Comput. Mater. 6 1
- [28] Li S, Pershin A, Thiering G, Udvarhelyi P and Gali A 2022 J. Phys. Chem. Lett. 13 3150
- [29] Tran T T, Elbadawi C, Totonjian D, Lobo C J, Grosso G, Moon H, Englund D R, Ford M J, Aharonovich I and Toth M 2016 ACS Nano 10 7331
- [30] Krečmarová M, Canet-Albiach R, Pashaei-Adl H, Gorji S, Muñoz-Matutano G, Nesládek M, Martínez-Pastor J P and Sánchez-Royo J F 2021 ACS Appl. Mater. Interfaces 13 46105
- [31] Wu F, Smart T J, Xu J and Ping Y 2019 Phys. Rev. B 100 081407(R)
- [32] Dev P 2020 arXiv:2002.05098

2D Mater. 10 (2023) 035036 S Zhang et al

- [33] Ping Y and Smart T J 2021 Nat. Comput. Sci. 1 646
- [34] Amblard D, D'Avino G, Duchemin I and Blase X 2022 arXiv:2204.11671 [cond-mat]
- [35] Wang D and Sundararaman R 2020 Phys. Rev. B 101 054103
- [36] Wang D and Sundararaman R 2019 Phys. Rev. Mater. 3 083803
- [37] Giannozzi P et al 2009 J. Phys.: Condens. Matter 21 395502
- [38] Perdew J P, Burke K and Ernzerhof M 1996 Phys. Rev. Lett. 77 3865
- [39] Schlipf M and Gygi F 2015 Comput. Phys. Commun. 196 36
- [40] Hamann D R 2013 Phys. Rev. B 88 085117
- [41] Smart T J, Li K, Xu J and Ping Y 2021 npj Comput. Mater. 71
- [42] Ping Y, Rocca D and Galli G 2013 Chem. Soc. Rev. 42 2437
- [43] Marini A, Hogan C, Grüning M and Varsano D 2009 Comput. Phys. Commun. 180 1392
- [44] Smart T J, Wu F, Govoni M and Ping Y 2018 Phys. Rev. Mater. 2 124002
- [45] Rozzi C A, Varsano D, Marini A, Gross E K U and Rubio A 2006 Phys. Rev. B 73 205119
- [46] Wu F, Rocca D and Ping Y 2019 J. Mater. Chem. C 7 12891
- [47] Guo C, Xu J, Rocca D and Ping Y 2020 Phys. Rev. B 102 205113
- [48] Guo C, Xu J and Ping Y 2021 J. Phys.: Condens. Matter 33 234001
- [49] Mackoit-Sinkevičienė M, Maciaszek M, Van de Walle C G and Alkauskas A 2019 Appl. Phys. Lett. 115 212101
- [50] Paleari F, Galvani T, Amara H, Ducastelle F, Molina-Sánchez A and Wirtz L 2018 2D Mater. 5 045017
- [51] Kirchhoff A, Deilmann T, Krüger P and Rohlfing M 2022 Phys. Rev. B 106 045118

- [52] Berseneva N, Gulans A, Krasheninnikov A V and Nieminen R M 2013 Phys. Rev. B 87 035404
- [53] Cassabois G, Valvin P and Gil B 2016 Nat. Photon. 10 262
- [54] Winter M, Bousquet M H E, Jacquemin D, Duchemin I and Blase X 2021 *Phys. Rev. Mater.* **5** 095201
- [55] Abdi M, Chou J-P, Gali A and Plenio M B 2018 ACS Photonics 5 1967
- [56] Gao S, Chen H-Y and Bernardi M 2021 npj Comput. Mater. 7 85
- [57] Hayee F et al 2020 Nat. Mater. 19 534
- [58] Xue Y, Wang H, Tan Q, Zhang J, Yu T, Ding K, Jiang D, Dou X, Shi J-j and Sun B-q 2018 ACS Nano 12 7127
- [59] Hod O 2012 J. Chem. Theory Comput. 8 1360
- [60] Krečmarová M, Canet Albiach R, Pashaei Adl H, Gorji S, Muñoz-Matutano G, Nesladek M, Martínez-Pastor J and Sánchez Royo J F 2021 ACS Appl. Mater. Interfaces 13 46105
- [61] Molina-Sánchez A, Catarina G, Sangalli D and Fernández-Rossier J 2020 J. Mater. Chem. C 8 8856
- [62] Tian T, Scullion D, Hughes D, Li L H, Shih C-J, Coleman J, Chhowalla M and Santos E J G 2020 Nano Lett. 20 841
- [63] Baroni S, de Gironcoli S, Corso A D and Giannozzi P 2001 Rev. Mod. Phys. 73 515
- [64] Bechstedt F 2015 Many-Body Approach to Electronic Excitations (Springer Series in Solid-State Sciences vol 181) (Berlin: Springer)
- [65] Neaton J B, Hybertsen M S and Louie S G 2006 Phys. Rev. Lett. 97 216405
- [66] Cho Y and Berkelbach T C 2018 Phys. Rev. B 97 041409
- [67] Towns J et al 2014 Comput. Sci. Eng. 16 62